Generating Dynamic Prescription Maps for Winter Road Treatment via Sun-Shadow Simulation

Yaguang Zhang[1], Sneha Jha[2], Darcy M. Bullock[3], and James V. Krogmeier[1]

Abstract—Snow and ice can severely decrease road transportation efficiency and cause deadly threats to drivers. To cope with this issue, a significant amount of workforce and resources are arranged for winter roadway treatments each year. These anti-icing treatments typically apply the same amount of chemicals along the entire section of roadway, regardless of how much roadway has direct exposure to the sun and how much roadway may be in shadows of vegetation or buildings. There is a need to develop systematic methods to identify sections of the road with significant shadows that reduce solar heating of the road and to generate custom maps that vary application rates according to presence of significant shadows. In this work, we present an open-source sun-shadow simulator capable of large-scale road analyses for dynamic prescription maps. The National Renewable Energy Laboratory's Solar Position Algorithm was used to estimate the time- and location-dependent incident angles of the Sun's rays, while state-wide LiDAR data from the United States Geological Services were utilized to locate obstacles. By comparing with on-site photos and satellite imagery, the simulation results were shown to be highly accurate. Furthermore, site-specific direct sun radiation energy values were evaluated for a 38-km-long highway segment as a case study. The resulting prescription maps make it possible to dynamically adjust pre-treatment amount at three-meter resolution, increasing efficiency and cost-effectiveness while reducing the environmental impact.

I. INTRODUCTION

Snow and ice on roads can greatly slow down the traffic and cause severe safety issues. Every year, a significant amount of workforce and resources are arranged to deal with this challenge. For example, the Indiana Department of Transportation (INDOT) considers snow and ice removal as their number one priority during the winter [1]. Besides mechanical means such as plowing, pre- and post-treatments of the road for anti- and de-icing are also among the most effective measures. However, it is common practice today to apply treatments such as brine solutions and various chlorides evenly over long road segments, although it has been long established that road surface in the shade suffers the snow and ice problem significantly more than that under

[1]Y. Zhang and J. V. Krogmeier are with the School of Electrical and Computer Engineering, Purdue University, 465 Northwestern Avenue, West Lafayette, IN 47907, USA. (Email: {ygzhang, jvk}@purdue.edu)
[2]S. Jha is with the Department of Agricultural and Biological Engineering, Purdue University, 225 South University Street, West Lafayette, IN 47907, USA. (Email: jha16@purdue.edu)
[3]D. Bullock is with the Lyles School of Civil Engineering, Purdue University, 550 West Stadium Avenue, West Lafayette, IN 47907, USA. (Email: darcy@purdue.edu)
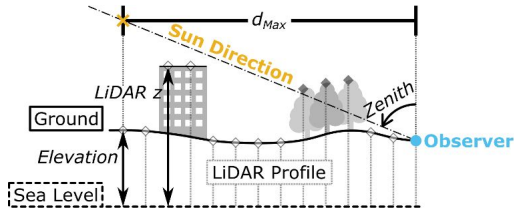
the sun [2]–[5]. More recently, [6] applied high-precision Digital Surface Model (DSM) derived from LiDAR data in shading pattern generation to model road surface temperature and they found that accumulated radiation could explain temperature differences better than instantaneous radiation. This LiDAR approach makes it possible to survey large areas in considerable detail and accordingly provide dynamic road treatment prescription maps for state-level operations.

In this paper, we present an open-source sun-shadow simulator [7] to generate large-scale dynamic prescription maps for winter road treatment operations. The simulator is written in Matlab and fully automated for roads in the state of Indiana. After the user specifies a road name, a mile marker range for the segment of interest, and a time range, the simulator is able to (i) extract surface polygons for the road segment of interest from public INDOT road information [8], [9], (ii) simulate time- and location-dependent direct sun radiation based on the National Renewable Energy Laboratory (NREL)'s Solar Position Algorithm (SPA) [10], and (iii) visualize the corresponding dynamic prescription maps in Google Earth [11] for easy user interactions. According to our best knowledge, we are the first group combining state-wide road and LiDAR information for large-scale dynamic prescription map generation. Our sun-shadow simulation achieves meter-level precision with a high accuracy. It could precompute the dynamic prescription maps for all roads in Indiana over the winter season as a baseline guidance to increase treatment efficiency and reduce environmental impact [12]. Post-treatment actions such as snow and ice removal could also benefit from these maps via proactive workforce deployment prioritizing high-risk road segments.

The paper is organized as follows. In Section II, we introduce the key ideas behind the sun-shadow simulator. Its implementation is described in Section III, followed by the performance evaluation in Section IV. A case study for a 38-km segment on U.S. Route 41 is presented in Section V. Finally, in Section VI, we conclude the paper.

II. DIRECT-PATH BLOCKAGE AND NORMALIZED SUN ENERGY

The simulator locates areas in the shade via a direct-path blockage model and estimates local heating effects for regions under the sun via a simplified sun radiation model.

A. Scenario Overview

Fig. 1 illustrates how the simulator determines whether an observer is in the Sun's shadow given the Sun's position. From the observer's location, a LiDAR z profile is obtained

Fig. 1. Illustration of the direct-path blockage scenario.

(a) Zenith is zero   (b) Zenith is non-zero   (c) Front view of (b)

Fig. 2. Power computation and normalization based on solar zenith angles.

toward the Sun's direction. For simplicity, the LiDAR z value for the observer is also used as their ground elevation. If any of the LiDAR z samples fall below the direct path between the observer and the Sun, as those for the trees in Fig. 1, that location is classified as *in the shadow*; otherwise, it is classified as *under the sun*.

Only a limited distance of the LiDAR data, denoted as d_{Max} in Fig. 1, needs to be inspected for computational consideration. Increasing d_{Max} will increase the computation needed for the simulation. However, if d_{Max} is too low, the accuracy of the simulation may decrease, especially for the case when the sun is at a low angle. For example, obstacles can cause extremely long shadows at sunset/sunrise. These obstacles may be missed with an insufficient d_{Max}.

Suppose we have 12 hours of daylight per day and the daytime solar zenith angle follows a continuous uniform distribution in time with a range between $-90°$ (sunrise) and $90°$ (sunset). Then, to ensure no obstacles shorter than $H_{obs} = 10\,\text{m}$ (a typical three-story building) will be missed except possibly during two time windows of $T_{win} = 15\,\text{min}$ (right after the sunrise and before the sunset, respectively), we would need a distance to inspect, d_{Max}, such that:

$$\arctan\left(H_{obs}/d_{Max}\right)/180° \times 12\,\text{h} \times 60\,\text{min}\,/\text{h} = T_{win}.$$

With the parameter values above, this gives us :

$$
\begin{aligned}
d_{Max} &= H_{obs}/\tan\left(T_{win}/720\,\text{min} \times 180°\right) \quad (1)\\
&= 10\,\text{m}/\tan\left(15\,\text{min}/720\,\text{min} \times 180°\right)\\
&\approx 152.57\,\text{m}
\end{aligned}
$$

Accordingly, d_{Max} is set to be $150\,\text{m}$ in the simulator.

B. Sun's Position and Obstacles

The simulator employs a Matlab implementation [13] of NREL's SPA [10] for estimating the solar zenith and azimuth angles based on the date, time, and location on Earth. This algorithm is highly accurate with uncertainties of +/−0.0003° in the period from the year −2000 to 6000 [10].

The Indiana 2016–2019 Statewide LiDAR data set [14] was used to locate obstacles including buildings and foliage. LiDAR profiles, as illustrated in Fig. 1, were generated by linearly interpolating 5-feet-resolution DSM files. A spatial resolution of $1.5\,\text{m}$ was chosen to match the DSM resolution.

C. A Simplified Direct Sun Radiation Model

We have assumed that any location of interest with a blocked direct path to the Sun receives no solar radiation. For othe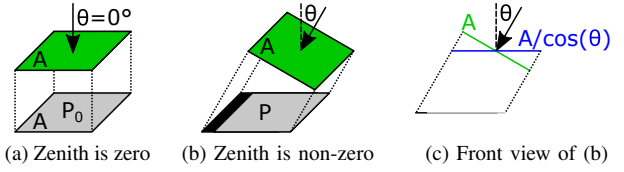r locations, as illustrated in Fig. 2, the absorbed solar power over unit ground area, denoted by P, can be computed and normalized based on the predicted solar zenith angle, θ, from SPA. When $\theta = 0°$, P peaks at P_0, and the normalized P, denoted by $\hat{P}$, should peak at one. In general,

$$P \cdot \frac{A}{\cos\theta} = P_0 \cdot A, \quad (2)$$

where A is a small reference area perpendicular to the Sun's rays. It is worth noting that P_0 does not change significantly throughout the year. Given the maximum and minimum distances, r_{Max} and r_{min}, from the Earth to the Sun [15],

$$
\begin{cases}
r_{Max} &= 152.099 \times 10^6 \text{ km}\\
r_{min} &= 147.092 \times 10^6 \text{ km},
\end{cases}
$$

we can estimate the relationship between the smallest and largest P_0 values, $P_{0,\,min}$ and $P_{0,\,Max}$, based on the free-space omnidirectional propagation model:

$$\frac{P_{0,\,min}}{P_{0,\,Max}} = \left(\frac{r_{min}}{r_{Max}}\right)^2 \approx 93.5\%. \quad (3)$$

This ratio will be closer to one for the winter season. Thus, we have assumed a constant P_0 value in the simulator. Accordingly, we have defined

$$\hat{P} = P/P_0 = \cos\theta. \quad (4)$$

With this simplified direct sun radiation model, the simulator is able to estimate the daily solar energy absorbed by unit ground area, $\hat{E}$, at a given location via trapezoidal integral of $\hat{P}$ values at a series of times for the date of interest. Note that $\hat{E}$ is also a normalized value, where $\hat{E} = 1$ corresponds to $E = P_0 \cdot 1\,\text{d} = P_0 \cdot 24\,\text{h}$. Intuitively, $\hat{E}$ peaking at one represents the maximum amount of solar heat one can get in one day by always staying right under the sun.

III. SIMULATOR IMPLEMENTATION

This section covers the technical details behind the sun-shadow simulator.

A. Structure Overview

A block diagram is provided in Fig. 3 as an overview of the simulator's structure. Before any simulation, the *geographic data preprocessor* processes the local copy of the Indiana DSM (LiDAR-derived) data by geographically indexing the raw files (43 423 .tif files in total; approximately 167 GB in size). This step makes it possible for the simulator to quickly identify the necessary files for any LiDAR profile generation. The preprocessor is also able to download and cache the 1/3rd arc-second terrain elevation data from the
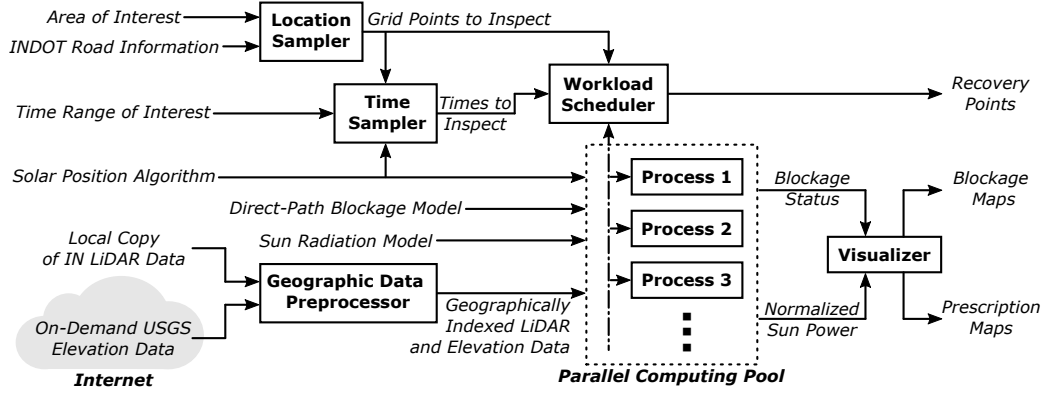
Fig. 3.   Block diagram of the sun-shadow simulator.

(a) Overview of road segments   (b) Grid points for one segment
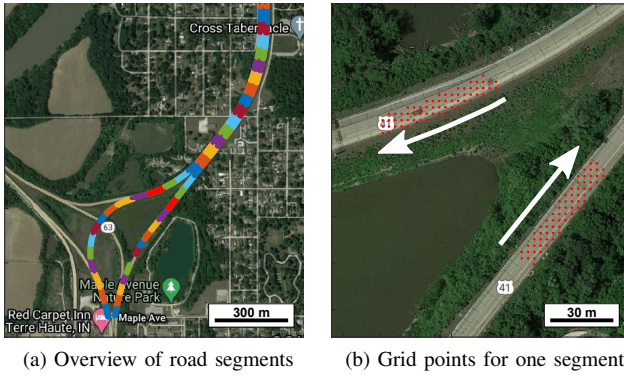
Fig. 4.   Illustrations of the road segmentation and the grid generation procedures for U.S. 41 on Google Maps (Plus Code: FHWQ+HC Terre Haute, Indiana).

United States Geological Services (USGS) as the fallback option for areas not covered by the LiDAR data set.

For each simulation, the location and time samplers determine the space-time grid points to consider. After the area/road of interest is specified by the user with a desired spatial resolution, the *location sampler* generates a grid covering the area accordingly. The location sampler is also able to (i) automatically generate a boundary polygon for the road of interest, and (ii) segment the road boundary into small polygons so that the simulation can be carried out by chunk. These procedures require the road information from INDOT, including mile markers [8] and street centerlines [9], as well as a predetermined lane width value. By default, the simulator assumes two-lane roads, creates the road outline with a lane width of $5\,\mathrm{m}$, divides the road into 50-m segments, and generates a grid with a spatial resolution of $3\,\mathrm{m}$ for each of the road segments.

Fig. 4 demonstrates that the simulator is flexible enough to work with polygons containing multiple regions and roads with separated lanes. From the road name with start and end points of interest, the location sampler automatically locates the road, divides it into small segments, and creates a simulation grid for each segment, as illustrated in Fig. 4(a). To achieve this, the simulator generated an interpolation function over available mile markers to translate GPS lo-

cations to mile marker values. This converted GPS data points into an ordered set, which was the key to properly breaking sides of the road boundary polygon for smaller road segments. Fig. 4(b) shows the 3-m-resolution grid for one of the 50-m road segments. As can be seen, the *grid points to inspect* cover the required road surface.

The *time sampler* uniformly extracts *times to inspect* from the local time range of interest, based on a desired time resolution for the shadow simulation. It also determines the local time zone for each grid point. This is necessary because roads could extend over multiple time zones but to the operators, the results would be significant as local time. Additionally, for each date covered by the time range of interest, the time sampler takes advantage of SPA to find the sunrise and sunset times for each grid point. Then, it informs the workload scheduler to skip night times accordingly.

The *workload scheduler* manages the overall simulation progress and periodically generates recovery points in case interruptions occur. The *processes* in the *parallel computing pool* compute the simulation based on the direct-blockage and the sun radiation models introduced in Section II. Finally, the *visualizer* aggregates the sun-shadow status and normalized sun power values from the parallel processes and generates maps for human operators.

B. Simulation Optimization

As a summary of this section, the following are the techniques we have applied in the sun-shadow simulator to optimize the performance and reduce the computational cost: 1) LiDAR data preprocessing, 2) limiting distance to inspect for obstacles, 3) adjustable time/space resolutions, 4) accurate road polygon generation, 5) skipping times in the night, and 6) parallel computing.

IV. SIMULATOR PERFORMANCE EVALUATION

Multiple experiments have been designed and completed to verify the performance of the simulator. This section highlights two of these to showcase the accuracy of the simulated sun shadow results.

A. On-Campus Tests

Blockages caused by buildings can form distinctive shadows with clear edges for easy comparison with the simulation

3389

(a) Photo taken at 4:08 p.m.

(b) Blockage map for 4:08 p.m.

(c) Photo taken at 5:01 p.m.

(d) Blockage map for 5:01 p.m.

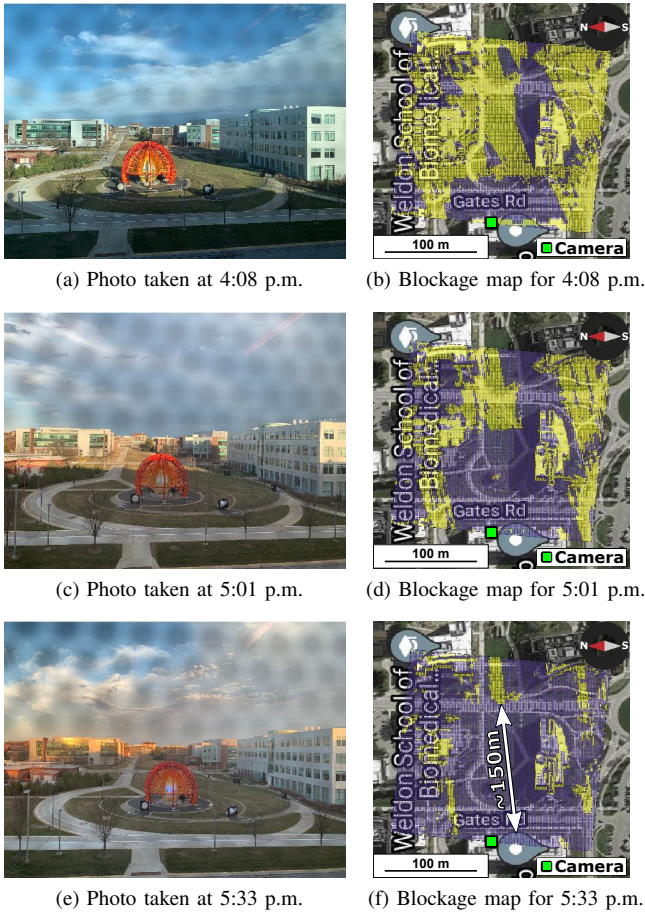(e) Photo taken at 5:33 p.m.

(f) Blockage map for 5:33 p.m.

Fig. 5. Example photos of building shadows at different times before the sunset, together with simulated blockage status for the same area overlaid on Google Maps (Plus Code: C3CG+PV West Lafayette, Indiana). On the blockage maps, locations in the shade are colored blue while locations under the sun are colored yellow.

(a) Grid points for the area of interest
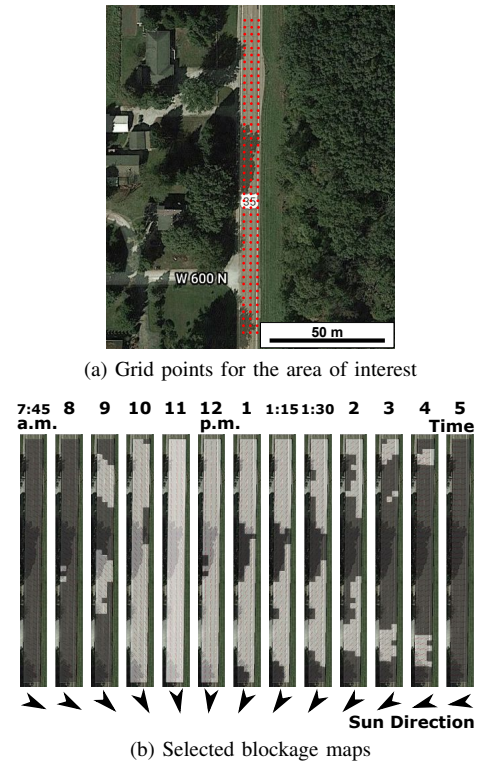
(b) Selected blockage maps

Fig. 6. Comparison between a satellite image from Google Maps and blockage results from the simulator. The satellite image was collected on Oct. 7, 2016. The simulation was run for the same date with a 15-min time resolution.

results. Three photos for the extension of a shadowed area from buildings before the sunset are included in Fig. 5, along with the corresponding simulation results. Photos of the VOSS Model were taken from the 3rd floor of the FLEX Lab building at Purdue University on Mar. 11, 2021. The grey dots on the photos were from the building glass, which should be ignored in the performance evaluation. Evidently, the shadowed areas from the simulator align perfectly with those recorded by the photos, proving the high accuracy of the sun-shadow simulator for building blockages at different times. It is worth noting that on Fig. 5(f), there is a narrow swath under the sun on the top of the map, which should instead be in the shade based on Fig. 5(e). However, this is expected because that region is more than $d_{Max} = 150$ m away from the obstacle, the FLEX building, on the bottom of Fig. 5(f). Increasing the distance to inspect, d_{Max}, will fix this issue, but as discussed in Section II-A, we chose not to do so considering the extra computational expense.

B. Comparison with Satellite Imagery

The VOSS model photos demonstrate the accuracy for the sun shadow simulator of the blockages caused by buildings
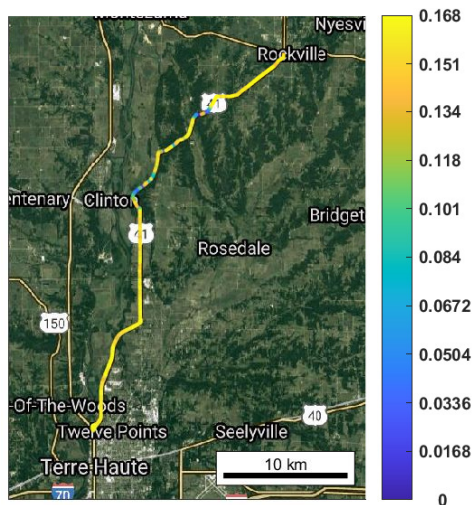
over different times, but there is not much foliage in that region of interest. We now simulate the screening effects of trees, which could significantly slow down the melting of snow/ice on the road surface. In Fig. 6, we look at a segment of State Road 35 where there is dense vegetation along both sides. Fig. 6(a) shows the grid points covering this 135-m-long road segment with a resolution of 3 m. The corresponding sun shadow outputs from the simulator are shown in Fig. 6(b). A perfect match between the simulation results at 1:15 p.m. and the satellite image can be observed, especially for the shadows cast by the trees on the left side of the road. Accordingly, we can conclude that the satellite image was captured at around 1:15 pm.
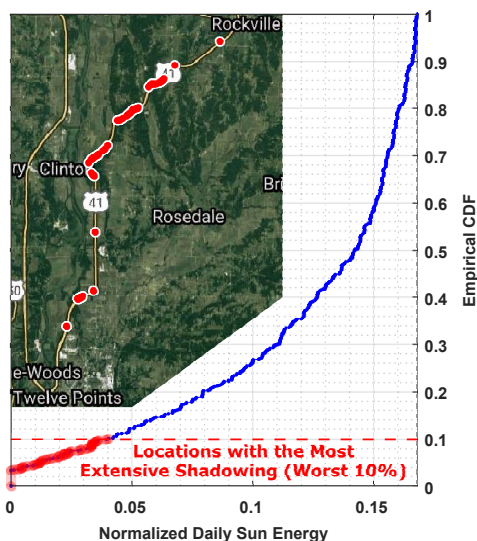
V. CASE STUDY FOR U.S. 41

The accurate shadow information from the simulator helps in identifying and locating high-risk segments which require more attention during winter road maintenance operations. In this section, we apply the sun-shadow simulator in dynamic prescription map generation for the U.S. 41 segment between Terre Haute and Rockville, Indiana.

A. Identifying Road Sections with Significant Shadows

As illustrated in Fig. 4, the road has been divided into small segments for high-resolution simulations. However, to quickly find high-risk locations, a low-resolution simulation for points along the road centerline was calculated. To build a grid for this simulation, we (i) split the road surface polygons from the road sampler, such that each resulting polygon has

3390

(a) Normalized daily sun energy

(b) The worst 10% locations

Fig. 7. A set of low-resolution simulations to locate high-risk locations for the 38-km U.S. 41 road segment between Terre Haute and Rockville, Indiana. The date of interest is Feb 11, 2021. The time resolution is 30 min. The spatial resolution for obtaining sample locations along the road is 50 m.

Fig. 8. Normalized daily sun energy values overlaid on Google Maps. The results are for the high-resolution grid of the road segment in Fig. 4.

B. High-Resolution Simulation and Treatment Distribution

For a stress test, we repeated the simulations with a 3-m resolution for the whole 38-km road. Fig. 8 plots the resulting normalized daily sun energy for one 50-m-long segment on the date of interest. Based on this information, dynamic prescription maps for variable treatment distribution can be generated. For example, the amount of brine solution needed by one unit area of the road should be reduced proportionally based on the amount of the sun energy expected to be absorbed.

These high-resolution simulations allow dynamic planning of treatment distribution not only along the road, but also perpendicular to the road along the width side, if the equipment allows such fine adjustments. If the treatment is applied by road segment, the simulation results can be aggregated for each segment to create corresponding dynamic prescription maps. For instance, the normalized daily sun energy values for points on the road segment of interest can be summed up to one value to vary the treatment applied for that segment compared with a reference amount.

For easier access to the large amount of simulation results, the visualizer of our simulator also interfaces with Google Earth [11] by exporting desired results into .kml files, as demonstrated by the screenshots in Fig. 9. Here, the ratio of grid points that are blocked in each road segment polygon is visualized by that polygon's transparency. The left-side *Places* pane in Fig. 9(a) has a list of all the blockage status polygons organized in different folders for different inspected times. The map view, shown in both screenshots, supports common interactions such as zooming and panning. A time bar is also provided on the top for sliding through the simulation results in time. A friendly visualization tool such as this one is the key to ensuring a high usability of the simulator in practice. These maps can be easily extended/improved with extra information, such as the real-time local weather, for a better performance. The simplified sun radiation model in the current simulator can also be updated with more complicated models.

only one region, and (ii) used the centroids of these polygons. The corresponding results are captured by Fig. 7. As can be seen in Fig. 7(a), the simulation results are aggregated as the normalized daily sun energy on Google Maps: the lower the energy, the higher the risk. With the help of the empirical cumulative distribution function (CDF) of the normalized daily sun energy values, we can conveniently locate the high-risk regions where the received direct sun radiation is limited, as plotted in Fig. 7(b). The locations with the least 10% radiation are plotted as an example.

The low-resolution simulation results can also be used to reduce the computation requirement for large-scale high-resolution simulations. For instance, by carrying out the high-resolution simulations only for the road segment polygons corresponding to the worst 10% locations shown in Fig. 7(b), we can reduce approximately 90% of the overall computation amount planned by the location sampler in Fig. 4.
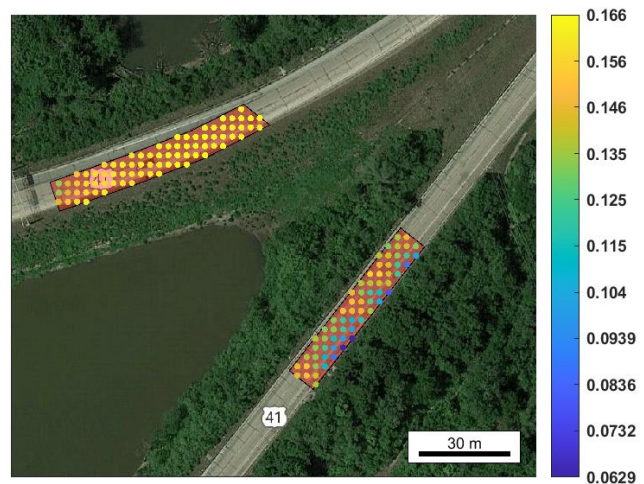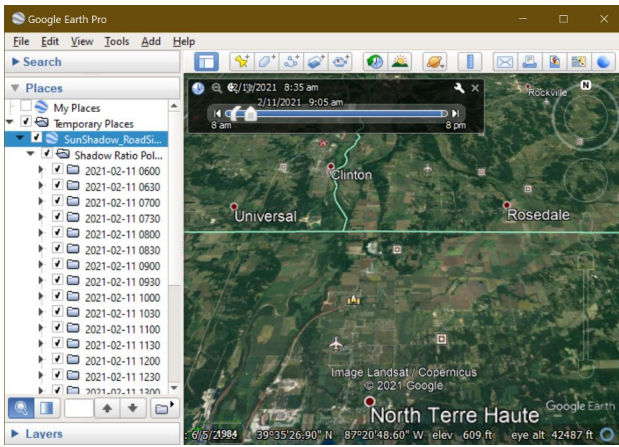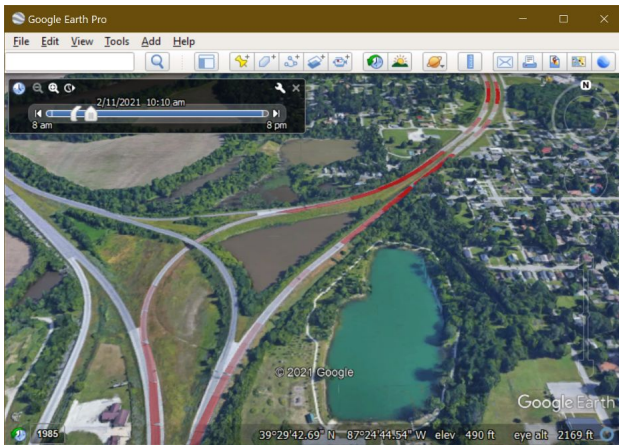
(a) Overview

(b) A zoomed-in view

Fig. 9. Simulation results loaded into Google Earth for better user interactions. The transparency of each road segment polygon was proportional to the ratio of unblocked grid points in that polygon: the red polygons are more visible if they have less blocked grid points.

VI. Conclusion

Shading significantly slows down the melting process of road snow and ice. High-precision LiDAR data make it possible to identify the Sun's shadows for large areas at a low cost. In this paper, we present a fully automated sun-shadow simulator to locate sections of road with the highest amount of shadowing. Through comparisons with real-life photos and satellite imagery, the simulator is shown to have a high accuracy. We also proposed a few visualization methods for analyzing the simulation results and accordingly generating dynamic prescription maps. These methods are flexible, user-friendly, and could guide road treatment for improved efficiency with reduced environmental impact.

In the future, we would like to run the simulator for larger road networks. Currently, on a 36-core cluster with 216 GB RAM, the low-resolution ($50\,\mathrm{m}/30\,\mathrm{min}$) simulation introduced in Section V-A took approximately $3\,\mathrm{h}$ to finish, while the high-resolution ($3\,\mathrm{m}/30\,\mathrm{min}$) simulation took approximately 13 days to finish. We will explore the possibility of decreasing the computational requirements by reusing (i) sun position results for nearby locations and

(ii) prescription maps for the same locations over reasonably short time intervals (e.g., one week). We would also like to take into consideration extra information, e.g., the degree of shading, weather, and obstacle types, for more accurate sun radiation results.

References

[1] "Winter operations," Indiana Department of Transportation, accessed: Apr. 7, 2021. [Online]. Available: https://www.in.gov/indot/3222.htm

[2] M. Milloy and J. Humphreys, "The influence of topography on the duration of ice-forming conditions on a road surface," Ministry Of Transport, London (UK), Tech. Rep., 1969.

[3] J. Bogren and T. Gustavsson, "Modelling of local climate for prediction of road slipperiness," *Physical Geography*, vol. 10, no. 2, pp. 147–164, 1989. [Online]. Available: https://doi.org/10.1080/02723646.1989.10642374

[4] J. Shao and P. J. Lister, "The prediction of road surface state and simulation of the shading effect," *Boundary-Layer Meteorology*, vol. 73, no. 4, pp. 411–419, Mar 1995. [Online]. Available: https://doi.org/10.1007/BF00712680

[5] J. Bogren, T. Gustavsson, M. Karlsson, and U. Postgård, "The impact of screening on road surface temperature," *Meteorological Applications*, vol. 7, pp. 97 – 104, 12 2006.

[6] Y. Hu, E. Almkvist, F. Lindberg, J. Bogren, and T. Gustavsson, "The use of screening effects in modelling route-based daytime road surface temperature," *Theoretical and Applied Climatology*, vol. 125, no. 1-2, pp. 303–319, Jul. 2016.

[7] Y. Zhang. (2021) Sun shadow simulator. GitHub. Accessed: Apr. 6, 2021. [Online]. Available: https://github.com/YaguangZhang/SunShadowSimulatorMatlabWorkspace

[8] "Mile-marker reference post inventory for roads in Indiana," Indiana Department of Transportation, 2015, accessed: Apr. 6, 2021. [Online]. Available: https://maps.indiana.edu/download/Infrastructure/Interstates_Mile_Markers_System1_INDOT.zip

[9] "Street centerlines maintained by county agencies in Indiana," Indiana Geographic Information Office, 2019, accessed: Apr. 6, 2021. [Online]. Available: http://maps.indiana.edu/download/Infrastructure/Streets_Centerlines_IGIO.zip

[10] I. Reda and A. Andreas, "Solar position algorithm for solar radiation applications," *Solar energy*, vol. 76, no. 5, pp. 577–589, 2004.

[11] *Google Earth*. (2021). Google LLC. Accessed: Apr. 7, 2021. [Online]. Available: https://www.google.com/earth/versions/

[12] C. A. Cooper, P. M. Mayer, and B. R. Faulkner, "Effects of road salts on groundwater and surface water dynamics of sodium and chloride in an urban restored stream," *Biogeochemistry*, vol. 121, no. 1, pp. 149–166, Oct 2014. [Online]. Available: https://doi.org/10.1007/s10533-014-9968-z

[13] M. Mahooti. (2021) NREL's Solar Position Algorithm (SPA). MATLAB Central File Exchange. Accessed: Apr. 6, 2021. [Online]. Available: https://www.mathworks.com/matlabcentral/fileexchange/59903-nrel-s-solar-position-algorithm-spa

[14] J. Jung and S. Oh. (2021) Indiana statewide normalized digital height model (2016-2019). Purdue University Research Repository. Accessed: Apr. 6, 2021. [Online]. Available: https://purr.purdue.edu/publications/3708/1

[15] D. R. Williams, "Earth fact sheet," NASA Goddard Space Flight Center, 2020, accessed: Apr. 6, 2021. [Online]. Available: https://nssdc.gsfc.nasa.gov/planetary/factsheet/earthfact.html